The pervasive presence of oxygen in ZrC

Daniel Hauser [a], Christoph Grießer [a], Eva-Maria Wernig [a], Thomas Götsch [a,c],
Johannes Bernardi [b], Julia Kunze-Liebhäuser [a], Simon Penner [a,*]

[a] *Institute of Physical Chemistry, University of Innsbruck, Innsbruck A-6020, Austria*
[b] *University Service Center for Transmission Electron Microscopy, TU Wien, Vienna A-1040, Austria*
[c] *Department of Inorganic Chemistry, Fritz-Haber Institute of the Max-Planck Society, Faradayweg 4–6, Berlin 14195, Germany*

ABSTRACT

Based on the recent interest in oxy-carbide materials in catalysis, we employ a thin film model concept to highlight that variation of key reaction parameters in the reactive magnetron sputtering of zirconium carbide films (sputtering power, template temperature or reactive plasma environment) under realistic preparation and application conditions often results in zirconium oxy-carbide films of varying stoichiometry. The composition of the films grown on silicon wafers and *in vacuo* - cleaved NaCl (001) single crystal facets was confirmed by depth profiling X-ray photoelectron spectroscopy and electron microscopy analysis. A correlation between methane-to-argon ratio, excess carbon and template temperature with elemental composition emphasizes the exclusive presence of oxygen-containing zirconium carbides. To generalize the approach, we also show that embedding of highly ordered Cu particles with uniform sizes in zirconium oxy-carbide matrices yields well-defined metal / oxy-carbide interfaces. As the presence of an oxy-carbide and its reactivity has been inextricably linked to enhanced activity and selectivity in a variety of processes, including hydrogenation, oxidation or reduction reactions, our model thin film approach provides the necessary well-defined catalysts to derive mechanistic details and to study the decomposition/re-carburization cycles of oxy-carbides. We have exemplified the concept for zirconium oxy-carbide, but deliberate extension to similar systems is easily possible.

1. Introduction

Transition metal carbides (TMCs) are known as a materials class exhibiting unique physical and chemical properties with applications in a wide range of research fields including heterogeneous and electro-catalysis [1,2]. The chemical and physical properties of these so-called interstitial alloys, i.e., solid mixtures of transition metals and carbon, strictly differ from those of the constituting metals and cause modifications of their structure and electronic, as well as reactivity properties. Transition metal carbides based on group 4–6 transition metals exhibit platinum metal group-like electric conductivity and heat capacity, which can be explained by a p-d hybridization due to a strong covalent bond between carbon and metal [3]. As for tungsten carbide, the strong covalent bonds of most other TMCs result in extreme hardness and brittleness, as well as in high melting points [4]. Some TMCs show catalytic characteristics like the platinum-group metals and thus, exhibit activity in reforming, hydrogenation processes or water-gas shift reaction [2,5,6]. Premise for electrocatalytic use of some transition metal

oxy-carbides, such as $ZrO_{0.31}C_{0.69}$, is essentially derived from the promising electrochemical stability over a wide potential or pH range [7]. Several electrochemical studies on C1 (e.g., CO or methanol) and C2 (ethanol) oxidation, hydrogen evolution or oxygen reduction reactions, proved their wide-scale application possibilities [8]. Despite these promising prospects, the performance of most of the TMCs is governed by their pronounced and unfavorable oxygen affinity and, thus, their tendency to form oxy-carbide compounds or thin oxide films at their surface that determine the reactivity at the solid/gas or solid/liquid interface [9]. In fact, there is an ongoing discussion about the true nature of the catalytically active centers during (electro-) catalytic operation of TMCs. Therefore, for full appreciation of the possibilities of using (oxy-)carbides as catalytic materials, the entire cycle of decomposition into carbide + oxide in oxidizing environments, as well as (oxy-)carbide re-formation in reducing atmospheres needs to be assessed. The archetypical oxy-carbide material, which has been in the center of attention, is titanium oxy-carbide TiO_xC_y. Most of its properties are already known and led to the conclusion, that it is a promising

---

* Corresponding author.
  E-mail address: simon.penner@uibk.ac.at (S. Penner).

material to replace carbon as support material in fuel cell applications at the solid/liquid interface [10]. Pt particles supported on titanium oxy-carbide exhibited enhanced ethanol oxidation properties, with the potential use as support in direct ethanol fuel cells [11]. This is mostly due to synergistic effects caused by the close proximity between suitable titania species and supported catalysts that can lead to an enhancement of the overall catalytic activity [12–14], which is often observed for compound materials. The carbides of tungsten and molybdenum (mostly WC, W_2C and Mo_2C) have shown an improved hydrogen evolution reactivity and have even been found to outperform noble metal catalysts in the gas-phase hydrogenation of CO_2 [15]. At least for Mo_2C, this beneficial behavior is due to the presence of a MoO_2 surface layer [9].

Recently, we have demonstrated the outstanding stability of a Zr oxy-carbide material, $ZrO_{0.31}C_{0.69}$, in reducing gasses, with only limited formation of ZrO_2 and pronounced electrochemical stability in acidic electrolytes – rendering the material a prospective candidate for electrocatalytic reactions at high anodic potentials, including carbon monoxide or even ethanol oxidation [7,16].

With respect to zirconium oxy-carbides, the parent zirconium carbide phase, ZrC, is a ceramic material with metallic character, and is mostly studied due to its ceramic properties, including high hardness, good wear resistance, high melting point or high optical emissivity [17, 18]. Electrochemical studies of ZrC, despite the relatively high electrical conductivity, are scarce, although bulk ZrC (possibly covered with a thin anodic oxide at the surface) as electrode material displays promising stability over a wide potential range for electrochemical oxidation processes [7,16] Of all TMC's, the oxo-philicity of ZrC represents the most serious obstacle [19]. As such, preparation of pure oxygen-free ZrC is not straightforward and usually, a respective oxy-carbide component is at least partially present. Literature reports stability of the Zr-oxy-carbides within the limits C/Zr = 0.64 and C/Zr = 0.98. Lower C/Zr ratios (i.e., higher oxygen contents) cause oxy-carbide decomposition into carbide and oxide. Recent work showed that the stoichiometry can be controlled via the synthesis protocol, allowing access to several zirconium oxy-carbides with the respective stoichiometries between C/Zr = 0.63 and C/Zr = 0.73 [7,16].

With respect to catalytic use in heterogeneous catalysts, the so-called material's gap, associated with the usual inability of inferring micro-kinetic mechanistic details from complex and ill-defined materials, still poses a serious obstacle in establishing structure-reactivity relationships [20]. The usual way out is the use of more defined model systems, making the elucidation of reaction mechanisms much easier [20]. In many cases, such model systems are thin film based and can, as simplified model systems, provide a more profound way to achieve a better understanding of the actual processes at the active sites of the catalyst surface [21,22]. This strategy is well-established for a number of materials classes relevant in catalytic research, including metals, oxides, intermetallic compounds or more complex entities such as metal-oxide composites [23–31]. Thin film systems for ZrC materials are well-known and have been in the focus from a ceramics point of view for decades, with respect to improving coating, hardness, friction or optical properties [29–47]. A range of depositions methods has been employed, including chemical vapor-deposition (mostly using methane) [30,33,35, 39,43,45], (reactive) magnetron sputtering [31,34] ion beam sputtering [36,37], pulsed laser ablation [32] or carburization techniques [41]. Target parameters are usually structure or morphology to steer the properties relevant for use as ceramic materials.

Although it is possible to prepare pure ZrC (thin) films under strict oxygen-free atmospheres, e.g., under ultra-high vacuum (UHV) conditions [48,49], one inherent problem not intentionally addressed in most of the thin film systems, is the oxy-carbide formation issue [19]. Of obvious tremendous importance for the understanding of the mechanistic details of the oxy-carbides' catalytic operation, the formation of simultaneous Zr-C and Zr-O bonds [33], as well as the dissolution of oxygen in ZrC matrices to change the optical properties of ZrC [36], are reported. The effect of oxygen impurities on the stability and structural

properties of ordered sub-stoichiometric ZrC_x was recently theoretically documented [50]. To illustrate the crucial importance of even minute amounts of oxygen present in transition metal carbide catalysts, recent results on complementary Mo_2C methane dry reforming [51] and CO_2 hydrogenation catalysts [52] have indicated that in fact a sub-monolayer oxygen coverage (e.g., of 0.67 ML [51]) represents the active state of the catalyst. There is, hence, ample evidence, that also trace amounts of oxygen in carbide materials significantly affect their properties.

To deliberately prepare Zr-oxy-carbide thin films with potential use as model systems in (electro-) catalytic research, we embarked on using reactive gas sputter experiments to obtain various thin film stoichiometric compositions of the target material [25,26], Hence, we show control of stoichiometry through use of specific synthesis protocols that can be steered via the preparation conditions. We have recently shown the carbon-free preparation of the ZrO_2 benchmark system [26]. The fully oxygen-free sample could not be prepared due to the extremely high oxygen affinity of ZrC and the associated high negative formation enthalpy of ZrO_2 ($\Delta H_f(ZrO_2) = -1100.6 \, kJ \, mol^{-1}$). The preparation and characterization is therefore highly influenced by parasitic oxidation processes. In this work, the stoichiometry of the films is steered by variation of substrate temperature, Zr sputter current, and methane/argon/oxygen ratio. We specifically also show the capabilities of our synthesis approach in the preparation of copper particles embedded in a Zr oxy-carbide matrix, giving rise to structural steering of the metal – oxy-carbide interface. Due to the well-defined copper particle size and local distribution, it represents a promising pathway for the synthesis of oxy-carbide - supported metal catalysts with potential use as new electrode materials for e.g., hydrogen generation. Metal/carbide interfaces are increasingly studied with respect to gas-phase and electro-catalytic applications [2,53–55]. To connect bulk and surface characterization, we rely on state-of-the-art electron microscopy and X-ray photoelectron spectroscopy evaluation.

2. Experimental

2.1. Zr oxy-carbide thin film preparation

All thin film preparation steps have been carried out using an ultra-flexible and highly modular vacuum setup, described in full detail in Ref. [25]. The core of the reactive magnetron sputtering setup is a quartz glass cross piece, to which the magnetron sputter device is attached, and which is pumped by a Leybold TURBOVAC 361 turbomolecular/ Leybold TRIVAC D16B rotary vane pump combination. A base pressure of 5 $\times 10^{-7}$ mbar is approached within 10 min of operation and measured by Pirani and ionization gage manometers. As relatively high pressures between 1×10^{-3} mbar and 1×10^{-2} mbar are required to ignite and maintain the argon plasma, throttling of the pumping speed and gas throughput by a gate valve was necessary to keep the turbo pump from a too high gas load. For reactive sputtering, two gas-dosing valves allow the introduction of various gasses into the chamber away from the plasma. To limit the reaction to the formed thin film, the gasses are therefore not introduced directly into the plasma. An additional gas port in the flange of the magnetron sputter source, connected to the gas injection ring of the sputter source, leads the sputter gas argon directly to the sputter target. This facilitates the ignition, keeps the plasma at much lower overall chamber pressures, and a higher pressure is only locally obtained. The magnetron sputter source is a Kurt J. Lesker Torus 2 HV, capable of operating targets of 50.8 mm in diameter. For the experiments discussed in this manuscript, the zirconium oxy-carbide films were deposited by reactive magnetron sputtering of a metallic Zr foil (Alfa Aesar 99.99%, 0.125 mm thickness) placed onto a metallic backing plate. Pure argon was supplied through the gas injection ring, while the rest of the chamber was backfilled with defined pressures of either methane or oxygen to eventually steer the composition of the resulting deposited thin film. All films were deposited onto polycrystalline Si

wafers at substrate temperatures between 300 °C and 500 °C, powers between 15 W and 50 W and total sputtering times between 30 min and 480 min.

In case of the preparation of Cu/Zr-oxy-carbide thin films, Cu was first deposited by thermal evaporation, followed by preparation of the zirconium oxy-carbide film as described above. The purity of the films on the Si wafers were checked by X-ray photoelectron spectroscopy survey scans and subjected to further structural and spectroscopic characterization. TEM samples were prepared by following a similar experimental procedure, but deposition was carried out on vacuum-cleaved NaCl (001) single crystal facets. Subsequent dissolution of NaCl in distilled water yielded self-supporting thin films suitable for transmission electron microscopy. This experimental approach, as well as the structural and spectroscopic correlation using different substrates has been documented in various studies over the past years [27,56,57].

2.2. Transmission electron microscopy

Elemental and structural analysis was performed by electron microscopy and EDX spectroscopy. The transmission electron microscopic (TEM) investigations were performed using a FEI TECNAI F20 field emission TEM operated at 200 kV, equipped with a high angle annular dark-field (HAADF) STEM detector, an Apollo XLTW SDD X-ray detector and a GATAN GIF Tridiem image filter. The spatial resolution of the EDX maps is about 1 nm. Electron energy loss spectroscopy was performed to study the chemical environment of Zr and to determine the film thickness.

2.3. X-ray photoelectron spectroscopy

A Thermo Scientific MultiLab 2000 spectrometer with an Alpha 110 hemispherical sector analyzer and a monochromatic Al K_α X-ray gun was employed for the XPS investigations ($E = 1486.4$ eV). A flood gun supplied electrons with a kinetic energy of 6 eV for charge compensation and the base pressure was kept in the low 10^{-9} mbar range.

High-resolution scans of the most relevant regions were recorded with a pass energy of 20 eV and an energy step size of 0.05 eV. For background correction, a Shirley-type function is utilized. The quantitative determination of the surface composition is based on high-resolution spectra of the Zr 3d and C 1s regions the relative sensitivity factors (RSFs). To account for the different inelastic mean free paths, the predictive G1 formula according to Gries [38] was utilized. Details regarding the fitting procedure are given in Tables 1 and 2.

The amount of ZrC$_x$, ZrO$_x$ and C$_{excess}$ was calculated from the overall atomic composition and the deconvoluted high-resolution (HR) spectra. Firstly, the amount of C$_{carbidic}$ and C$_{excess}$ was calculated from the deconvoluted C 1s spectra:

$$C_{Carbidic}(at.\%) = C_{carbidic}(Fit) * C(at.\%)$$

$$C_{Excess}(at.\%) = C_{Excess}(Fit) * C(at.\%)$$

The atomic fraction of ZrO$_x$ was, thus, calculated as follows:

$$Zr_{oxidic}(at.\%) = (100 - Zr_{Carbidic}(Fit)) * \frac{Zr\ (at.\%)}{100}$$

This directly leads to the normalized atomic ratios of the species, e.g.

$$ZrC_x = 100 * \frac{C_{Carbidic}(at.\%)}{C_{Carbidic}(at.\%) + C_{Excess}(at.\%) + Zr_{oxidic}(at.\%)}$$

All thin films were used in the as-prepared state. No Ar sputtering to remove native oxygen layers from the films has been performed to limit the impact of Ar sputtering on the thin film composition.

3. Results

3.1. Challenges in the preparation of zirconium oxy-carbide films

With respect to the understanding of zirconium oxy-carbide materials and films, special focus was put on elucidating the micro-kinetic reaction steps. It is now accepted, that ZrC$_x$ is sub-stoichiometric in carbon ($0.7 < x < 0.98$) [58,59], and that the carbo-thermal reduction of ZrO$_2$ leads to a zirconium oxy-carbide species [41]. In these compounds, the oxygen atoms are found in the octahedral position of the Zr lattice and are stepwise substituted by carbon [42,59,60]. The resulting stoichiometry ZrO$_x$C$_y$ is strongly dependent on the synthesis conditions (e.g., temperature or partial pressure of reactants) [41]. These considerations are equally important for the thin film preparation pathway discussed in this manuscript. Due to the strong getter effect of zirconium, we expect the carburization of (sub-stoichiometric) ZrO$_{2-x}$ and the formation of the ZrO$_x$C$_y$ as reported for the carburization of powder ZrO$_2$ [61] instead of direct carburization of zirconium metal. The detailed reaction mechanism of ZrO$_2$ is complex, and several intermediate Zr oxy-carbide species are reported before the final ZrO$_x$C$_y$ stoichiometry is reached. It involves two major steps, the reductive carburization of ZrO$_2$ and the subsequent carbon oxidation to CO. The latter reaction is crucial, as especially excess carbon formation is common in zirconium carbide thin films. Also, the presence of additional ZrO$_{2-x}$ phases has been reported [62,63].

In summary, the challenges to reproducibly prepare zirconium oxy-carbide films with a continuous stoichiometry are considerable and it is of utmost importance to pinpoint the surface and bulk stoichiometry by e.g., dedicated XPS quantification through sputter depth profiling.

3.2. Correlation of zirconium oxy-carbide stoichiometry with key sputter parameters: Surface chemical analysis and depth profiling by X-ray photoelectron spectroscopy

To highlight the capability of our approach, Fig. 1 exhibits a full set

Table 1
Detailed XPS fitting parameters and constraints of the high-resolution (HR) spectra of Fig. 3.

Sample		Position [FWHM] / eV							
CH$_4$	Position	Zr$_{carbidic,5/2}$	Zr$_{carbidic,3/2}$	Zr$_{oxidic,5/2}$	Zr$_{oxidic,3/2}$	Zr$_{suboxidic,5/2}$	Zr$_{suboxidic,3/2}$	C$_{excess}$	C$_{carbidic}$
5	Surface	179.3 [1.2]	181.7 [1.2]	182. 5 [1.5]	184.9 [2.5]	n.d.	n.d.	285.0 [1.6]	281.5 [0.8]
5	Bulk	179.3 [1.1]	181.7 [1.1]	182.5 [2.0]	184.9 [2.0]	180.6 [1.9]	183.0 [1.0]	n.d.	282.0 [1.4]
10	Surface	179.3 [1.2]	181.7 [1.2]	182.4 [1.6]	184.8 [1.6]	n.d.	n.d.	284.9 [1.6]	281.6 [1.2]
10	Bulk	179.3 [1.2]	181.7 [1.2]	182.3 [2.0]	184.7 [2.0]	180.6 [2.0]	183.0 [2.0]	284.2 [1.6]	282.0 [1.2]
15	Surface	139.3 [1.2]	181.7 [1.2]	182.1 [1.5]	184.5 [1.5]	n.d.	n.d.	284.5 [1.6]	281.8 [1.2]
15	Bulk	179.3 [1.1]	181.7 [1.1]	182.6 [2.0]	185.0 [2.0]	180.5 [2.0]	182.9 [2.0]	284.1 [1.6]	282.2 [1.2]
20	Surface	139.3 [1.2]	181.7 [1.2]	182.1 [1.5]	184.5 [1.5]	n.d.	n.d.	284.4 [1.5]	281.4 [1.2]
20	Bulk	139.3 [1.2]	181.7 [1.2]	182.3 [2.0]	184.7 [2.0]	180.8 [2.0]	183.2 [2.0]	284.2 [1.7]	282.2 [1.1]
Constraints	Lineshape	GL(30)0T(1.3)	GL(30)T(1.3)	GL(30)	GL(30)	GL(30)	GL(30)	GL(30)	GL(30)T(1.3)
	Assymmetry	0.335	0.335	0	0	0	0	0	0.335
	Binding Energy	179.3	Zr$_{,5/2}$ + 2.4	arbitrary	Zr$_{,5/2}$ + 2.4	arbitrary	Zr$_{,5/2}$ + 2.4	arbitrary	arbitrary
	FWHM	0.9 – 1.2	Zr$_{,5/2}$ * 1	1.4 – 2.0	Zr$_{,5/2}$ * 1	1.4 – 2.0	Zr$_{,5/2}$ * 1	1.5 – 1.7	0.8 – 1.4

Table 2
Detailed fitting parameter and constraints of the high-resolution XP spectra presented in Fig. 4.

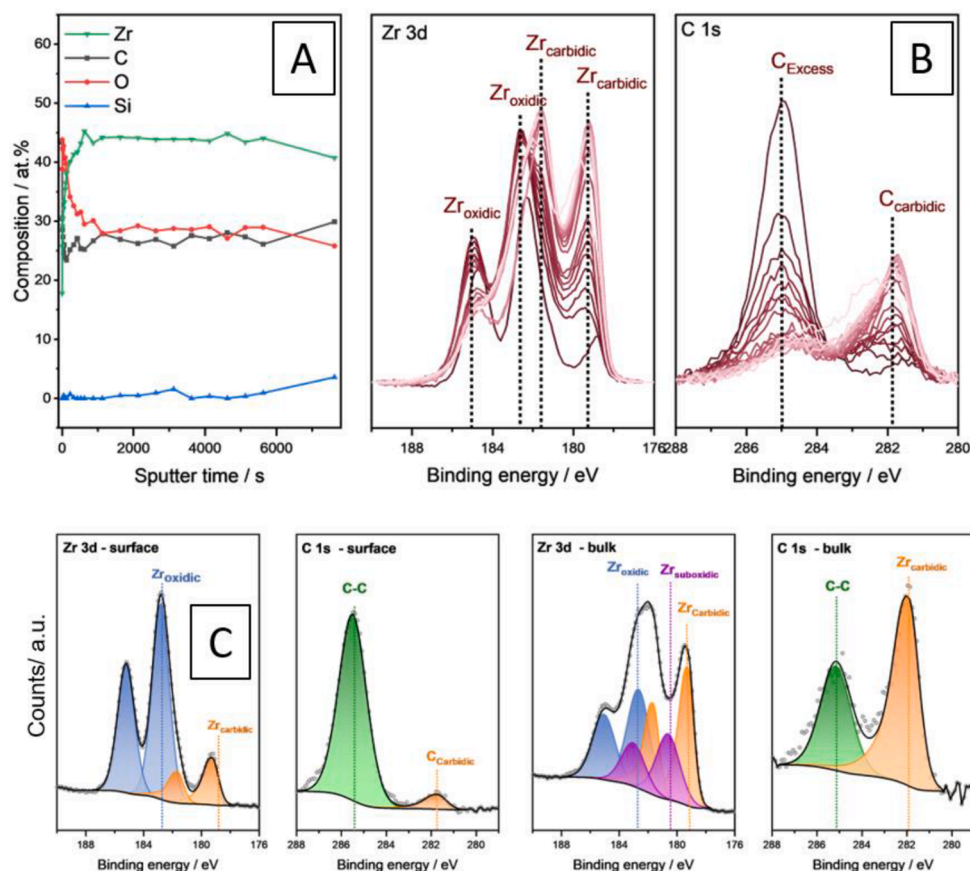| Sample		Position [FWHM] / eV							
T / °C	Position	$Zr_{carbidic,5/2}$	$Zr_{carbidic,3/2}$	$Zr_{oxidic,5/2}$	$Zr_{oxidic,3/2}$	$Zr_{suboxidic,5/2}$	$Zr_{suboxidic,3/2}$	C_{excess}	$C_{carbidic}$
300	Surface	179.3 [1.2]	181.7 [1.2]	182.5 [1.5]	184.9 [2.5]	n.d.	n.d.	285.0 [1.6]	281.5 [0.8]
300	Bulk	179.3 [1.1]	181.7 [1.1]	182.5 [2.0]	184.9 [2.0]	180.6 [1.9]	183.0 [1.0]	n.d.	282.0 [1.4]
500	Surface	179.3 [1.1]	181.7 [1.1]	182.8 [1.4]	185.2 [1.4]	n.d.	n.d.	285.5 [1.6]	281.7 [1.0]
500	Bulk	179.3 [1.0]	181.7 [1.0]	182.7 [1.8]	185.1 [1.8]	180.6 [1.9]	183.0 [1.9]	285.1 [1.6]	281.9 [1.1]
Constraints	Lineshape	GL(30)0T(1.3)	GL(30)T(1.3)	GL(30)	GL(30)	GL(30)	GL(30)	GL(30)	GL(30)T(1.3)
	Assymmetry	0.335	0.335	0	0	0	0	0	0.335
	Binding Energy	179.3	$Zr_{,5/2}$ + 2.4	arbitrary	$Zr_{,5/2}$ + 2.4	arbitrary	$Zr_{,5/2}$ + 2.4	arbitrary	arbitrary
	FWHM	0.9 – 1.2	$Zr_{,5/2}$ * 1	1.4 – 2.0	$Zr_{,5/2}$ * 1	1.4 – 2.0	$Zr_{,5/2}$ * 1	1.5 – 1.7	0.8 – 1.4

Fig. 1. Full set of X-ray photoelectron spectroscopy analysis data for a representative zirconium oxy-carbide film deposited under the following conditions: $P_{magnetron}$ = 30 W, p_{CH4} = 5 × 10^{-4} mbar, T = 500 °C. Panel A: Depth profile of the film composition; Panel B: Sequence of high-resolution Zr 3d and C 1s XP spectra collected at different sample depths from the surface (dark red lines) to around 200 nm (light red lines); Panel C: Direct comparison of surface and bulk high-resolution Zr 3d and C 1s XP spectra including deconvolution into Zr_{oxidic} (blue), $Zr_{Carbidic}$ (orange), $Zr_{suboxidic}$ (violet), C-C (green) and $C_{carbidic}$ (orange) species to highlight the presence of individual components.

of surface-chemical analysis alongside depth profiling of a representative zirconium oxy-carbide thin film using exemplary fixed preparation conditions ($P_{magnetron}$ = 30 W, p_{CH4} = 5 × 10^{-4} mbar, T = 500 °C). This analysis has been performed for all thin films discussed in this manuscript. Fig. 1A shows the depth profiling data that were acquired in sequential sputtering steps and Panel B a set of high-resolution Zr 3d and C 1s XP spectra, that were used to identify the individual components of each element. In Panel C, the exemplary deconvolution into individual species is highlighted. Possible preferential sputtering effects in this system selectively removing reactive oxygen from ZrO_2 targets during depth profiling, leading to partially reduced ZrO_{2-x} species, are explicitly taken into account and fitted in all XPS data analysis [25]

As a first result, as derived from the exemplary fits used for the detailed analysis of the film shown in Fig. 1, we note that the concentration of oxygen and carbon at the surface is around 15 at.% higher as compared to the bulk, while the amount of zirconium at the surface is substantially lower than in the bulk. We address this to adsorption of oxygenate species during contact to ambient while transferring the samples from the magnetron sputtering device to the X-ray

spectrometer. However, at a certain sample depth of around 5 nm (corresponding to ~1000s sputter time), the atomic concentrations of all elements almost saturate and indicate a uniform Zr-O-C composition. This is a general trend for all zirconium oxy-carbide thin films. The same effect is visible in the high-resolution Zr 3d and C 1s XP spectra (Panel B). The purely oxidic Zr component has diminished considerably after 1000s of sputtering and is gradually replaced by an oxy-carbidic Zr species, as also in deeper regions a considerable oxygen concentration is prevalent. After 1000s of sputtering, the thin film composition reaches a steady value also in the high-resolution spectra. The terms "carbidic" and "oxidic" are hereby used to emphasize the dominant character of the respective compound and should not be viewed as either pure carbide or oxide. The same trend is observed in the C 1s spectra, where the carbidic component also rises upon sputtering to deeper layers. Excess carbon, which represents unreacted surface-bound carbon from the preparation and transfer processes also vanishes in deeper layers. A clear change from a surface stable oxidic Zr phase ($Zr3d_{5/2}$ at 182.5 eV and $Zr3d_{3/2}$ at 185 eV) with excess sp3 carbon (C1s at 284.9 eV) to a more carbidic ($Zr3d_{5/2}$ at 179.3 eV and $Zr3d_{3/2}$ at 181.7 eV) bulk region is observed

[35,64,65].

The deconvoluted high-resolution spectra in Panel C display the difference between surface (left side) and bulk (right side) and include all present component fits. Oxide-related peak fits were conducted with a convoluted Gauss-Lorentz GL(30) function, while carbide related peaks have been fitted with the asymmetrical function GL(30)T(1.3). More details are given in Section 2.3. The overall picture is hereby the same as in the waterfall plots in Panel B, but the deconvolution allows better determination of the chemical state of Zr and C. Additionally to the expected oxide and carbide related signals, also peaks assigned to Zr sub-oxidic Zr species arise, which result from preferential reactive oxygen sputtering. Although we are aware of the fact, that especially for thin film/interfacial ZrO_{2-x} species several sub-stoichiometric components can be discriminated [66], we opted to fit all sub-stoichiometric ZrO_{2-x} species in our case with one Zr 3d doublet only without losing essential information. As preferential sputtering of carbon or zirconium is not an issue under the preparation conditions applied here [26,67] and surface and bulk spectra are shown and accordingly discussed in internal comparison only, the quantification of the species is reliable. The O1s signal (Fig. 2) clearly reveals the presence of oxygen in all layers/depths of the film.

The systematic extension of the parameter room for the carbothermal conversion to different methane-to-argon ratios and template temperatures is highlighted in the following to show the universality of the oxy-carbide formation concept, based on complete sets of XP spectra used for this evaluation in Figs. 3 and 4 (top row). The resulting quantification of the thin film composition is given in Figs. 3 and 4 Panel A–C (bottom row), respectively.

To highlight the dependence of the ZrO_xC_y stoichiometry on the methane concentration (Fig. 3 Panel A–C), the methane concentration was increased from $p_{CH4}:p_{Ar}$ = 5:95 to 20:80 (see Fig. 1). The sputtering power and template temperature were kept constant ($P_{magnetron}$ = 50 W,
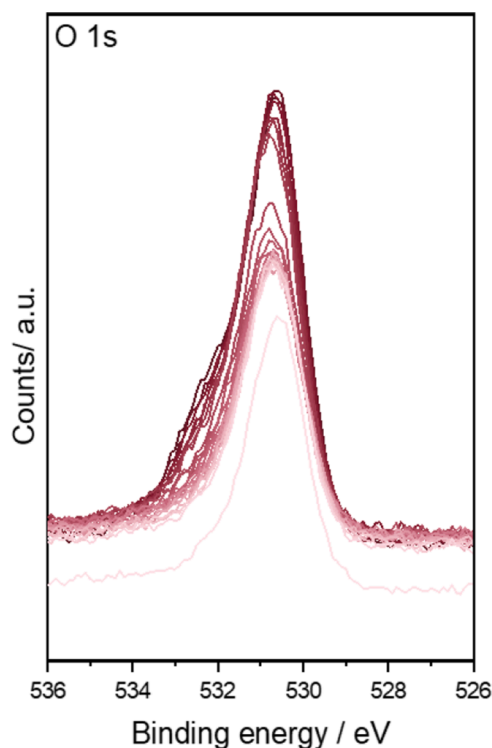

Fig. 2. O 1s waterfall plot for a zirconium carbide thin film deposited at following conditions: $P_{magnetron}$ = 30 W, pCH_4 = 5 × 10^{-4} mbar, T = 500 °C (cf. Fig. 1). The sputter time increases from 0 s (darkest red line, surface) to around 7500 s (sample depth around 200 nm, lightest red line). Color code for depth variation as in Fig. 1.

$T_{substrate}$ = 300 °C). As expected, higher methane concentrations result in more excess carbon both at the surface, as well as in the bulk, as inferred from the respective C 1s region (left side of the graph). The surface composition appears comparably constant, whereas more changes are observed in bulk regions, i.e., in deeper layers the $Zr_{carbidic}$: Zr_{oxidic} ratio rises along with the excess carbon with increasing methane concentration. At the highest methane concentrations, more excess carbon in relation to carbide is expectedly present. The same trend is observed in the Zr 3d spectra. Both oxidic and carbidic Zr components are visible at the surface and in deeper layers of the film. The respective quantification is summarized in Table 3.

At higher methane concentrations, excess carbon is increasingly dominant in bulk regions, ranging from 0 at.% at 5% methane to 57.7 at. % at 20% methane. At similar sputter speeds, this indicates that not all carbon can be converted into an oxy-carbide by reaction with zirconium, despite the high sputter power and argon partial pressure. The bulk zirconium oxy-carbide content is accordingly decreasing. The best conversion, i.e., lowest amount of excess carbon with at the same time highest oxy-carbide content, is reached at the lowest methane concentration of 5%. As it is essentially devoid of bulk excess carbon, it represents pure zirconium oxy-carbide in the bulk. Interestingly, the ratio of $Zr_{carbidic}$:Zr_{oxidic} changes drastically with increasing methane concentration: it increases from 1.2 at 5% methane to ~1.5 at 10% methane, to ~ 2.2 at 15% methane and 3.4 at 20% methane. As the most important information from the methane variation series, we note that even under strong carburizing conditions at the highest methane concentrations, oxygen is still detected in the deepest sputtered layers (at around 100 nm). This directly confirms the presence of zirconium oxy-carbide in the bulk.

The results, thus, indicate an oxy-carbide surface layer, which is more oxidic than carbidic in nature. Due to the propensity of zirconium to form a very stable passivating oxide layer upon contact to air [68], this is reasonable. This logically follows from the fact that the cubic zirconium carbide structure is known to be only stable as a sub-stoichiometric compound, creating a high number of defect sites acting as possible oxidation sites [69,70]. We never detected pure zirconium carbide at the surface under ambient conditions. Most importantly, at all methane concentrations and even after depth profiling, zirconium is never present as a pure carbide, but rather as an oxy-carbide in the bulk. The oxidation of zirconium carbide on the surface is known to proceed via microscopic cracks and pores [71], which render deeper layers also accessible to oxidation. It also has been reported that the pervasive presence of oxygen in the structure, i.e., the presence of oxy-carbides, represents a pre-state before full oxidation to ZrO_2 [72]. Putting these results into literature perspective, two major obstacles are generally present in zirconium oxy-carbide (thin film) material characterization. Firstly, it is not straightforward to structurally distinguish ZrC_x and ZrC_xO_y due to their similar structural properties. Secondly, oxygen contamination must be completely suppressed to synthesize pure zirconium carbide, which is notoriously hard to avoid [70]. For the industrially most common carbo-reduction route to powder zirconium carbide, it is proposed that the obtained product is rather an oxy-carbide phase with oxygen atoms located at the octahedral position within the zirconium carbide lattice (therefore representing a solid solution of ZrO and ZrC) [41]. Based on our results, this seems to be also the case for sputtered ZrC thin films, which are still mostly declared as pure zirconium carbide films in literature, despite the clear presence of oxidized zirconium carbide species [18,31,34,37,73,74]. This insight has been indicated in some studies [69,71], and is validated by our findings.

The influence of the template temperature on the composition of zirconium oxy-carbide thin films has been exemplarily assessed quantitatively for template temperatures of 300 °C and 500 °C (Fig. 4, quantification in Table 2 and 3). The bulk spectra reveal more carbidic zirconium and additional Zr sub-oxides, while the respective surface spectra generally display more excess carbon and completely oxidized
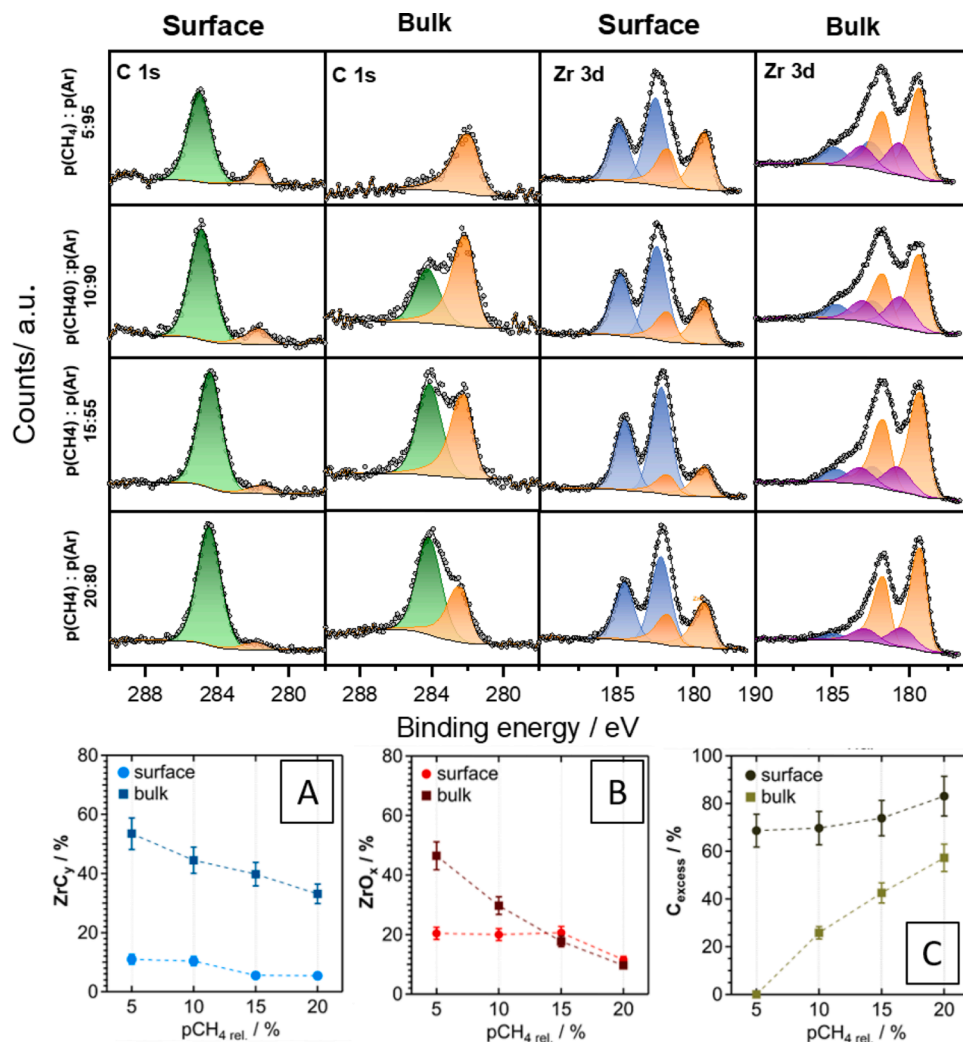
Fig. 3. Top row: XPS overview chart of zirconium oxy-carbide thin films grown with different methane-to-argon ratios. Topmost row: p_{CH4}:p_{Ar} = 5:95; second row from the top: p_{CH4}:p_{Ar} = 10:90; third row from the top: p_{CH4}:p_{Ar} = 15:85; bottom row: p_{CH4}:p_{Ar} = 20:80. Surface and bulk spectra (at around 20 nm depth) of the C1s and Zr 3d region are deconvoluted to highlight the Zr_{oxidic} (blue), $Zr_{Carbidic}$ (orange), $Zr_{suboxidic}$ (violet), C-C (green) and $C_{carbidic}$ (orange) species present in the thin films. Bottom row: Panel A – C: Detailed quantitative analysis of the X-ray showing the dependence of the zirconium oxy-carbide stoichiometry on the methane concentration. Fixed synthesis parameters: $P_{magnetron}$ = 50 W and $T_{substrate}$ = 300 °C.

zirconium. The film deposited at 300 °C shows substantially higher carbide signals compared to that deposited at 500 °C, which reveals more excess carbon. Both surface and bulk compositions vary with varying template temperature. Especially the bulk composition analysis at 500 °C reveals a lower reaction rate towards zirconium oxy-carbide and ~20 at-% excess carbon, while no excess carbon is detected at 300 °C. We tentatively address this phenomenon to the complex deposition mechanism during reactive magnetron sputtering of metal carbides and its strong temperature dependence [31]. However, apart from the mechanistic details, which are not yet understood in full detail, we emphasize that all zirconium carbide species were always accompanied by bulk oxygen, either as (sub)oxide or interstitially bonded oxygen. This zirconium oxy-carbide material is present under all preparation conditions, especially in the bulk.

3.3. Structural and morphological characterization

Structural characterization of the zirconium oxy-carbide thin films is essentially based on electron microscopy. Fig. 5 highlights the TEM characterization for two representative sets of Zr-O-C thin film preparation. All films are represented by a small-grain structure (Fig. 5A) with a low contrast in the TEM images. The previously discussed excess carbon is also visible, decorating the film edges (marked by a black arrow). As indicated in Fig. 5B, the films are mostly polycrystalline, and over extended patches, distinct lattice fringes with a spacing of ~2.7 Å indicate the presence of the (111) lattice planes of the parent cubic ZrC

structure. The EEL spectrum shown as inset in Fig. 3B closely matches that of an oxidized zirconium compound in the oxidation state +4. As we have laid out in the previous section, all films without exception feature the presence of (bulk) oxygen typically within a few sputtered layers. This is now directly corroborated by the HAADF/EDX mapping experiments shown in Fig. 5C and D. While the interpretation of the HAADF is not straightforward and mostly shows thickness variations, the EDX mapping with the overlay of the Zr-K, O-K and C-K edge intensities reveals a homogeneous distribution of all constituting elements, strongly pointing towards a zirconium oxy-carbide phase. Therefore, the lattice fringes in Panels B are assigned a zirconium oxy-carbide, not ZrC, in line with the XPS results discussed above. As the zirconium oxy-carbide structure is mainly derived from an elongation of the lattice constants of ZrC due to the interstitial oxygen, the unambiguous assignment solely based on the lattice spacings analysis is difficult. Only by combination with XPS and EDX, the presence of the zirconium oxy-carbide structure is directly revealed.

To extend the characterization and to further show the strength of our thin film approach, we have deliberately used the zirconium oxy-carbide thin films as matrix to embed small metal particles and to thus, create a defined metal-zirconium oxy-carbide interface. Due to the potential use as electro-catalytic material, we have opted for copper as a first metal to provide the proof-of-principle.

The electron microscopy analysis of the Cu/zirconium oxy-carbide composite is outlined in Fig. 6. Fig. 6A reveals the outstandingly ordered array of sphere-shaped Cu particles with a size of around 5 nm and
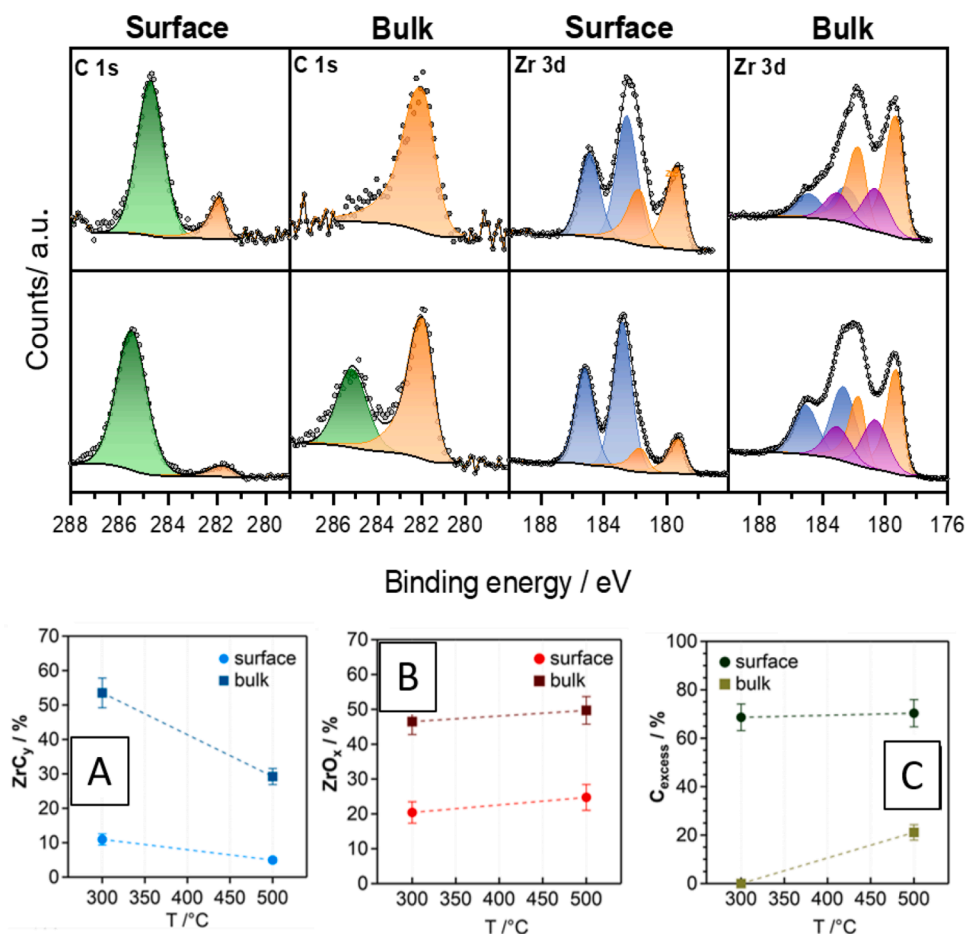
Fig. 4. Top row: XPS overview chart for the zirconium oxy-carbide thin film series resulting from template temperature variation at 300 °C (topmost row) and 500 °C (second row from the top). The surface and bulk spectra (at a depth of 20 nm) for C 1 s and Zr 3d are shown alongside their deconvolution, respectively. Bottom row: Panel A – C: Detailed quantitative analysis of the X-ray photoelectron spectra showing the dependence of the zirconium oxy-carbide stoichiometry on the template temperature. Lines between points are shown as guide to the eye. Fixed synthesis parameters: $P_{magnetron} = 50$ W and $p_{methane} = 5 \times 10^{-4}$ mbar.

Table 3

Quantification of the XP spectra series collected for the methane pressure and template temperature variation as shown in Figs. 3 and 4.

Methane Concentration Variation				Template Temperature Variation			
surface bulk /atomic ratio%				surface bulk /atomic ratio%			
CH_4 /%	$Zr_{carbidic}$	Zr_{oxidic}	C_{excess}	T /°C	$Zr_{carbidic}$	Zr_{oxidic}	C_{excess}
5	11.0	20.4	68.6	300	11.0	20.4	68.6
	53.5	46.5	0		53.5	46.4	0
10	10.4	20.0	69.7	500	5.0	24.8	70.3
	44.5	29.7	25.8		29.2	49.7	21.1
15	5.5	20.6	73.9				
	39.8	17.7	42.6				
20	5.4	11.5	83.1				
	33.1	9.7	57.2				

grains, which are accordingly decorated with the Cu particles. Again, the EDX mapping strongly suggests the presence of a zirconium oxy-carbide and not ZrC, as the Zr-K, O-K and C-K intensities follow the HAADF derived morphology, and their locations match very closely. The Cu-K intensity map reveals a slightly higher intensity at the grain boundaries of the tetrahedral crystallites, suggesting these as the predominant attachment locations.

4. Conclusions

Varying the preparation parameters during reactive magnetron sputtering preparation of zirconium carbide without exception results in zirconium oxy-carbide film formation. It is extremely difficult under typical preparation and typical application conditions to prepare a pure Zr carbide. Although pure Zr carbide films can be prepared under strictly oxygen-free atmospheres, by reviewing the relevant literature, we suggest that the presence of a zirconium oxy-carbide is very likely in many cases, even if the samples are in fact termed "zirconium carbide". The reason is the very close structural match of the cubic zirconium carbide and a zirconium oxy-carbide with oxygen located at interstitial sites. We suggest that the surface is inherently oxidized, whereas the bulk is composed of zirconium oxide and a solution of zirconium sub-oxides and carbide ("zirconium oxy-carbide"), with a pervasive presence of oxygen throughout the thin film.

As the decomposition of the oxy-carbide under oxidative environments and the (partial) re-carburization in reductive environments is at the epicenter of catalytic activity, the results will provide a guideline for use of such oxy-carbide materials in heterogeneous- and electro-catalysis. For structure-activity correlations, the use of model systems is imperative. The pure and Cu-modified zirconium oxy-carbide thin
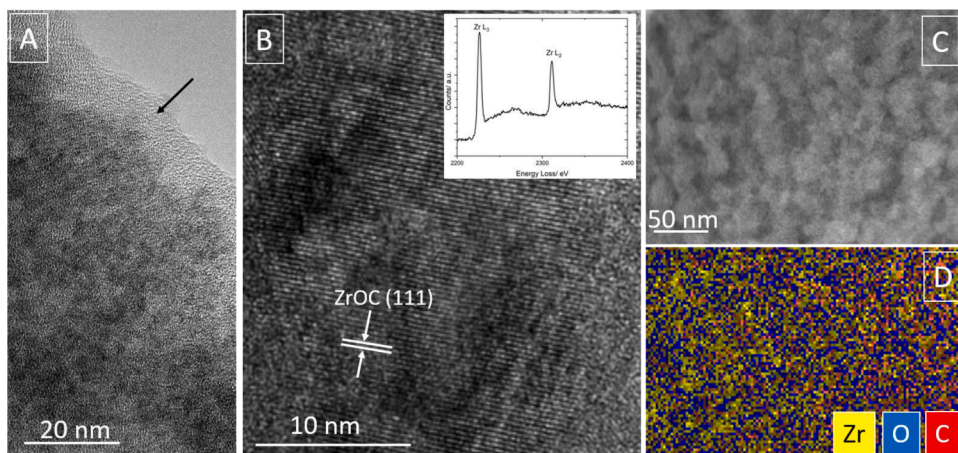
the peculiar triangular-shaped morphology of the zirconium oxy-carbide matrix. This is best seen in the insets in Fig. 6A (bright-field image upper right corner, HAADF image in the lower left corner). As we deposit Cu on the NaCl (001) cleave faces before embedding them in the zirconium oxy-carbide matrix and all structures exhibit cubic lattices, we might speculate about the epitaxial stabilization of this triangular structure by the pre-deposited Cu. High-resolution imaging (Fig. 4B) reveals Cu (111) lattice spacings on the round particles and zirconium oxy-carbide (111) lattice fringes on the triangular grains. The presence of the latter is also revealed in the SAED patterns shown as inset. Due to the high ordering of both Cu and zirconium oxy-carbide, the interface is also well-ordered and perfectly suited to study its properties from a mechanistic point of view. In fact, the HAADF image in Panel C even exposes the regular three-dimensional tetrahedral shape of the zirconium oxy-carbide

Fig. 5. Electron microscopy characterization of pure and self-supporting Zr oxy-carbide thin films (P = 30 W, $T_{template}$ = 500 °C, p_{CH4}:p_{Ar} = 10:90). Panel A: Bright-field overview TEM image of the thin edge of a zirconium oxy-carbide film. The amorphous excess carbon decorating the film edge is marked by a black arrow. Panel B: High-resolution image of the zirconium oxy-carbide displaying (111) reflections. Inset: Electron-energy loss spectrum of the zirconium oxy-carbide film. **Panel C:** HAADF image of the zirconium oxy-carbide film. Panel D: EDX mapping of the film shown in Panel E using an overlay of Zr-K (yellow), O–K (blue) and C–K (red) edge intensities. The scale bar in Panel C also applies to Panel D.
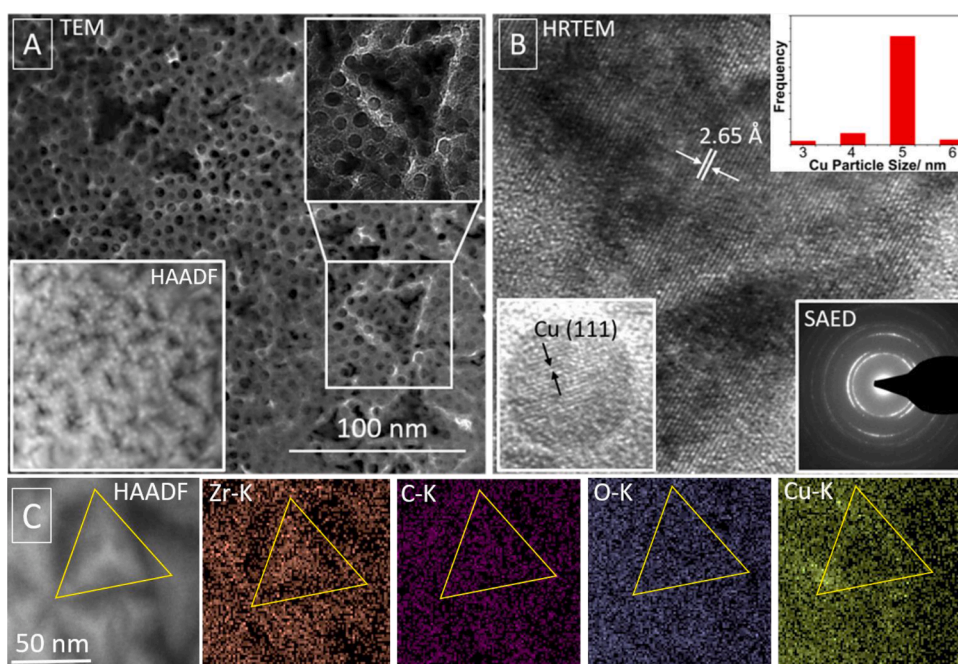
Fig. 6. Structural and spectroscopic TEM characterization of the Cu-zirconium oxy-carbide thin film (parameters for the zirconium oxy-carbide thin film: P = 30 W, $T_{template}$ = 500 °C, p_{CH4}:p_{Ar} = 10:90). Panel A: Overview TEM image. Insets show an enlarged view of one Cu-decorated triangular-shaped ZrO_xC_y grain, as well as the corresponding HAADF image of the same region. Panel B: High-resolution images of a single triangular-shaped zirconium oxy-carbide grain (main Panel), as well as a Cu particle (inset). The SAED pattern is featured in the lower right corner alongside a particle size statistic based on the count of 100 particles in the upper right corner. Panel C: STEM-EDX analysis of the Cu-zirconium oxy-carbide thin film based on the Zr-K, C-K, O-K and Cu-K intensities. The yellow triangle marks the same tetrahedral zirconium oxy-carbide particle. Template temperature of Cu deposition: 500 °C.

films with highly defined metal/oxy-carbide interface are perfect models in this respect and allow for easy preparation and extension to similar metal – oxy-carbide materials.

CRediT authorship contribution statement

Daniel Hauser: Formal analysis. **Christoph Grießer:** Formal analysis. **Eva-Maria Wernig:** Formal analysis. **Thomas Götsch:** Formal analysis. **Johannes Bernardi:** Formal analysis. **Julia Kunze-Liebhäuser:** Supervision. **Simon Penner:** Supervision, Writing – original draft, Project administration.

Declaration of Competing Interest

The authors declare that they have no known competing financial interests or personal relationships that could have appeared to influence the work reported in this paper.

Data Availability

Data will be made available on request.

Acknowledgments

References

[1] Q. Zhang, L. Pastor-Pérez, S. Gu, T.R. Reina, Transition metal carbides (TMCs) catalysts for gas phase CO_2 upgrading reactions: a comprehensive overview, Catalysts 10 (2020) 955, https://doi.org/10.3390/catal10090955.

[2] M. Kuang, W. Huang, C. Hegde, W. Fang, X. Tan, C. Liu, J. Ma, Q. Yan, Interface engineering in tansition metal carbides for electrocatalytic hydrogen generation and nitrogen fixation, Mater. Horiz. 7 (2020) 32–55, https://doi.org/10.1039/C9MH01094G.

[3] M.E. Eberhart, J.M. MacLaren, S.T. Oyama, The Chemistry of Transition Metal Carbides and Nitrides, Springer Netherlands, Dordrecht, 1996, pp. 107–120.

[4] Toth, Refractory Materials Series L.E. Toth, Refractory Materials Series, 7, Academic Press, New York and London, 1971, p. 91.

[5] R.B. Levy, M. Boudart, Platinum-like behavior of tungsten carbide in surface catalysis, Science 181 (1973) 547–549, https://doi.org/10.1126/science.181.4099.547.

[6] Y. Lee, J.H. Ahn, H.Y. Park, J. Jung, Y. Jeon, D.G. Lee, M.H. Kim, E. Lee, C. Kim, Y. Kwon, H.W. Lee, J.H. Jang, J.H. Lee, H.K. Song, Support structure-catalyst electroactivity relation for oxygen reduction reaction on platinum supported by two-dimensional titanium carbide, Nano Energy 79 (2021), 105363, https://doi.org/10.1016/j.nanoen.2020.105363.

[7] N. Shakibi Nia, D. Hauser, L. Schlicker, A. Gili, A. Doran, A. Gurlo, S. Penner, J. Kunze-Liebhäuser, Zirconium oxycarbide: a highly stable catalyst material for electrochemical energy conversion, ChemPhysChem 20 (2019) 3067–3073, https://doi.org/10.1002/cphc.201900539.

[8] W. Wan, B.M. Tackett, J.G. Chen, Reactions of water and C1 molecules on carbide and metal-modified carbide surfaces, Chem. Soc. Rev. 46 (2017) 1807–1823, https://doi.org/10.1039/C6CS00862C.

[9] C. Griesser, et al., True nature of the transition-metal carbide/liquid interface determines its reactivity, ACS Catal. 11 (2021) 4920–4928, https://doi.org/10.1021/acscatal.1c00415.

[10] J. Kunze-Liebhäuser, C. Rüdiger, Titanium oxycarbides: formation, properties and application in electrocatalysis, refer. module in chemistry, Mol. Sci. Chem. Eng. 10.1016/B978-0-12-409547-2.14136-8.

[11] N. Nia, et al., DEMS studies of the ethanol electro-oxidation on TiOC supported Pt catalysts–Support effects for higher CO_2 efficiency, Electrochim. Acta 304 (2019) 80–86, https://doi.org/10.1016/j.electacta.2019.02.089.

[12] L. Xiong, A. Manthiram, Synthesis and characterization of methanol tolerant Pt/TiOx/C nanocomposites for oxygen reduction in direct methanol fuel cells, Electrochim. Acta 49 (2004) 4163–4170, https://doi.org/10.1016/j.electacta.2004.04.011.

[13] Y. Liu, T.G. Kelly, J.G. Chen, W.E. Mustain, Metal carbides as alternative electrocatalyst supports, ACS Catal. 3 (2013) 1184–1194, https://doi.org/10.1021/cs4001249.

[14] M. Roca-Ayats, G. García, M.A. Peña, M.V. Martínez-Huerta, Titanium carbide and carbonitride electrocatalyst supports: modifying Pt–Ti interface properties by electrochemical potential cycling, J. Mater. Chem. A 2 (2014) 18786–18790, https://doi.org/10.1039/C4TA03782K.

[15] C. Rüdiger, J. Brumbarov, F. Wiesinger, S. Leonardi, O. Paschos, C. Valero Vidal, J. Kunze-Liebhäuser, Ethanol oxidation on TiOxCy-supported Pt nanoparticles, ChemCatChem 5 (2013) 3219–3223, https://doi.org/10.1002/cctc.201300217.

[16] D. Hauser, A. Auer, J. Kunze-Liebhäuser, S. Schwarz, J. Bernardi, S. Penner, Hybrid synthesis of zirconium oxycarbide nanopowders with defined and controlled composition, RSC Adv. 9 (2019) 3151–3156, https://doi.org/10.1039/C8RA09584A.

[17] V. Craciun, E.J. McCumiskey, M. Hanna, C.R. Taylor, Very hard ZrC thin films grown by pulsed laser deposition, J. Eur. Ceram. Soc. 33 (2013) 2223–2226, https://doi.org/10.1016/j.jeurceramsoc.2013.01.001.

[18] A. Gilewicz, K. Mydłowska, J. Ratajski, Ł. Szparaga, P. Bartosik, P. Kochmański, R. Jędrzejewski, Structural, mechanical and tribological properties of ZrC thin films deposited by magnetron sputtering, Vacuum 169 (2019), 108909, https://doi.org/10.1016/j.vacuum.2019.108909.

[19] A.L. Stottlemyer, T.G. Kelly, Q. Meng, J.G. Chen, Reactions of oxygen-containing molecules on transition metal carbides: surface science insight into potential applications in catalysis and electrocatalysis, Surf. Sci. Rep. 67 (2012) 201–232, https://doi.org/10.1016/j.surfrep.2012.07.001.

[20] Mind the gap, editorial, Nat. Catal. 1 (2018) 807–808, https://doi.org/10.1038/s41929-018-0188-0.

[21] S. Penner, Pure and mixed-oxide thin film model systems grown on sodium chloride templates for structural and catalytic studies, Thin Solid Films 562 (2014) 1–15, https://doi.org/10.1016/j.tsf.2014.03.001.

[22] J. Sauer, H.J. Freund, Models in catalysis, Catal. Lett. 145 (2015) 109–125, https://doi.org/10.1007/s10562-014-1387-1.

[23] H.J. Freund, M. Bäumer, J. Libuda, T. Risse, G. Rupprechter, S. Shaikhutdinov, Preparation and characterization of model catalysts: from ultrahigh vacuum to *in situ* conditions at the atomic dimension, J. Catal. 216 (2003) 223–235, https://doi.org/10.1016/S0021-9517(02)00073-8.

[24] P. Lackner, J. Hulva, E.M. Köck, W. Mayr-Schmölzer, J.I.J. Choi, S. Penner, U. Diebold, F. Mittendorfer, J. Redinger, B. Klötzer, G.S. Parkinson, M. Schmid, Water adsorption at zirconia: from the ZrO2(111)/Pt3Zr(0001) model system to powder samples, J. Mater. Chem. A 6 (2018) 17587–17601, https://doi.org/10.1039/C8TA04137G.

[25] T. Götsch, E.M. Wernig, B. Klötzer, An ultra-flexible modular high vacuum setup for thin film deposition, Rev. Sci. Instrum. 90 (2019), 023902, https://doi.org/10.1063/1.5065786.

[26] T. Götsch, B. Neumann, B. Klötzer, S. Penner, Substoichiometric zirconia thin films prepared by reactive sputtering of metallic zirconium using a direct current ion beam source, Surf. Sci. 680 (2019) 52–60, https://doi.org/10.1016/j.susc.2018.10.015.

[27] T. Götsch, W. Wallisch, M. Stöger-Pollach, B. Klötzer, S. Penner, From zirconia to yttria: sampling the YSZ phase diagram using sputter-deposited thin films, AIP Adv. 6 (2016), 025119, https://doi.org/10.1063/1.4942818.

[28] T. Götsch, D. Hauser, N. Köpfle, J. Bernardi, B. Klötzer, S. Penner, Complex oxide thin films: pyrochlore, defect fluorite and perovskite model systems for structural, spectroscopic and catalytic studies, Appl. Surf. Sci. 452 (2018) 190–200, https://doi.org/10.1016/j.apsusc.2018.05.019.

[29] H. Lorenz, C. Rameshan, T. Bielz, N. Memmel, W. Stadlmayr, L. Mayr, Q. Zhao, S. Soisuwan, B. Klötzer, S. Penner, From oxide-supported palladium to intermetallic palladium phases: consequences for methanol steam reforming, ChemCatChem 5 (2013) 1273–1285, https://doi.org/10.1002/cctc.201200712.

[30] S. Bira, T.T. Thabete, T.T. Hlatshwayo, H. Bissett, T. Ntsoane, J.B. Malherbe, Investigating the thermal stability of the chemical vapor deposited zirconium carbide layers, J. Alloy. Compd. 834 (2020), 155003, https://doi.org/10.1016/j.jallcom.2020.155003.

[31] S.S. Kumar, A. Sharma, G.M. Rao, S. Suwas, Investigations on the effect of substrate temperature on the properties of reactively sputtered zirconium carbide thin films, J. Alloy. Compd. 695 (2017) 1020–1028, https://doi.org/10.1016/j.jallcom.2016.10.225.

[32] L. D'Alessio, A. Santagata, R. Teghil, M. Zaccagnino, I. Zaccardo, V. Marotta, D. Ferro, G. De Maria, Zirconium carbide thin films deposited by pulsed laser ablation, Appl. Surf. Sci. 168 (2000) 284–287, https://doi.org/10.1016/S0169-4332(00)00625-5.

[33] Y. Sun Won, Y. Kim, V.G. Varanasi, O. Kryliouk, T.J. Anderson, C.T. Sirimanne, L. McElwee-White, Growth of ZrC thin films by aerosol-assisted MOCVD, J. Cryst. Growth 304 (2007) 324–332, https://doi.org/10.1016/j.jcrysgro.2006.12.071.

[34] Q.N. Meng, M. Wen, F. Mao, N. Nedfors, U. Jansson, W.T. Zheng, Deposition and characterization of reactive magnetron sputtered zirconium carbide films, Surf. Coat. Technol. 232 (2013) 876–883, https://doi.org/10.1016/j.surfcoat.2013.06.116.

[35] P.C. Wang, Y.S. Li, K.A.R. Mitchell, XPS studies of the stability of a zirconium carbide film in the presence of zirconium oxide and hydrogen, Surf. Rev. Lett. 2 (1995) 297–303, https://doi.org/10.1142/S0218625X95000315.

[36] A. Singh, M.H. Modi, A.K. Sinha, R. Dhawan, G.S. Lodha, Study of structural and optical properties of zirconium carbide (ZrC) thin films deposited by ion beam sputtering for soft X-ay optical applications, Surf. Coat. Technol. 272 (2015) 409–414, https://doi.org/10.1016/j.surfcoat.2015.03.033.

[37] A. Singh, M.H. Modi, R. Dhawan, G.S. Lodha, Structure and composition of zirconium carbide thin-film grown by ion beam sputtering for optical applications, Solid State Phys. 1591 (2014) 869–871, https://doi.org/10.1063/1.4872785.

[38] W.H. Gries, A universal predictive equation for the inelastic mean free pathlengths of X-ray photoelectrons and auger electrons, Surf. Interface Anal. 24 (1996) 38–50, https://doi.org/10.1002/(SICI)1096-9918(199601)24, 1<38::AID−SIA84>3.0.CO;2-H.

[39] Y. Wang, Q. Liu, J. Liu, L. Zhang, L. Cheng, Deposition Mechanism for chemical vapor definition of zirconium carbide coatings, J. Am. Ceram. Soc. 91 (2008) 1249–1252, https://doi.org/10.1111/j.1551-2916.2007.02253.x.

[40] C. Chen, C. Liu, C. Tsao, Influence of growth temperature on microstructure and mechanical properties of nanocrystalline zirconium carbide films, Thin Solid Films 479 (2005) 130–136, https://doi.org/10.1016/j.tsf.2004.11.196.

[41] J. David, G. Trolliard, M. Gendre, A. Maitre, TEM study of the reaction mechanisms involved in the carbothermal reduction of zirconia, J. Eur. Ceram. Soc. 33 (2013) 165–179, https://doi.org/10.1016/J.JEURCERAMSOC.2012.07.024.

[42] F. Rejasse, O. Rapaud, G. Troillard, O. Masson, A. Maitre, Experimental investigation and thermodynamic evaluation of the C-O-Zr ternary system, RSC Adv. 102 (2016) 100122–100135, https://doi.org/10.1039/C6RA21967E.

[43] G.H. Reynolds, Chemical vapor deposition of ZrC on Pyrocarbon-coated fuel particles, J. Nucl. Mater. 50 (1974) 215–216, https://doi.org/10.1016/0022-3115(74)90158-5.

[44] T.B. Xie, W.A. Mackie, P.R. Davies, Field Emission from ZrC Films on Si and Mo single emitters and emitter arrays, J. Vac. Technol. B14 (1996) 2090–2092, https://doi.org/10.1116/1.588876.

[45] C.M. Hollabaugh, L.A. Wahmann, R.d. Reiswig, T.C. Wdace, J.M. White, P. Wagner, Chemical vapor deposition of ZrC made by reactants of ZrCl4 with CH_4 and with C_3H_6, Nucl. Technol. 35 (1977) 527–535, https://doi.org/10.13182/NT77-A31913.

[46] V.G. Samoilenko, L.N. Pereselentseva, Deposition of zirconium carbide coating acting as diffusion barrriers in composites consisting of a metallic matrix and refractory metal fibres, Powder Metall. Met. Ceram. 14 (1975) 725–7728, https://doi.org/10.1007/bf00800241.

[47] C.M. Hollabaugh, L.A. Wahmann, R.d. Reiswig, T.C. Wdace, J.M. White, P. Wagner, Factors influencing the chemical vapor deposition of ZrC, J. Nucl. Mater. 62 (1976) 221–228, https://doi.org/10.1016/0022-3115(76)90018-0.

[48] H. Zaid, A. Alemann, K. Tanaka, C. Li, P. Berger, T. Back, J. Fankhauser, M. S. Goorsky, S. Kodambaka S, Influence of ultra-low ethylene partial pressure on microstructural and compositional evolution of sputter-deposited Zr-C thin films, Surf. Coat. Technol. 398 (2020), 126053, https://doi.org/10.1016/j.surfcoat.2020.126053.

[49] G. Greczynski, D. Primetzhofer, L. Hultman, Reference binding energies of transition metal carbides by core-level x-ray photoelectron spectroscopy free from Ar+ etching artefacts, Appl. Surf. Sci. 436 (2018) 102–110, https://doi.org/10.1016/j.apsusc.2017.11.264.

[50] T. Davey, Y. Chen, The effect of oxygen impurities on the stability and structural properties of vacancy-ordered and-disordered ZrCx, RSC Adv. 12 (2022) 3198–3215, https://doi.org/10.1039/d1ra07768f.

[51] A. Kurlov, E.B. Deeva, P.M. Abdala, D. Lebedev, A. Tsoukalou, A. Cormas-Vives, A. Fedorov, C.R. Müller, Exploiting two-dimensional morphology of molybdenum oxycarbide to enable efficient catalytic dry reforming of methane, Nat. Commun. 11 (2020) 4920, https://doi.org/10.1038/s41467-020-18721-0.

[52] H. Zhou, Z. Chen, E. Kountoupi, A. Tsoukalou, P.M. Abdala, P. Florian, A. Fedorov, C.R. Müller, Two-dimensional molybdenum carbide 2D-Mo₂C as a superior catalyst for CO₂ hydrogenation, Nat. Commun. 12 (2021) 5510, https://doi.org/10.1038/s41467-021-25784-0.

[53] J. Rodriguez, Activation of gold on metal carbides: novel catalysts for C1 chemistry, Front. Chem. 7 (2020) 875–886, https://doi.org/10.3389/fchem.2019.00875.

[54] J. Li, et al., Two-dimensional transition metal carbides as supports for tuning the chemistry of catalytic nanoparticles, Nat. Commun. 9 (2018) 5258, https://doi.org/10.1038/s41467-018-07502-5.

[55] Z. Zhao, Insight into the formation of Co@Co₂C catalysts for direct synthesis of higher alcohols and olefins from syngas, ACS Catal. 8 (2018) 28–41, https://doi.org/10.1021/acscatal.7b02403.

[56] T. Götsch, L. Mayr, M. Stöger-Pollach, B. Klötzer, S. Penner, Preparation and characterization of epitaxially grown unsupported yttria-stabilized zirconia (YSZ) thin films, Appl. Surf. Sci. 331 (2015) 427–436, https://doi.org/10.1016/j.apsusc.2015.01.068.

[57] R. Thalinger, M. Pollach, B. Klötzer, S. Penner, Thin film model systems of ZrO₂ and Y₂O₃ as templates for potential industrial applications investigated by electron microscopy, Mater. Chem. Phys. 138 (2013) 384–391, https://doi.org/10.1016/j.matchemphys.2012.11.071.

[58] A. Ouensaga, M. Dode, Study of oxygen solubility in zirconium carbide at 1555°C with free carbon and thermodynamical equilibrium conditions, Rev. Int. Hautes Temp. Refract. 11 (1974) 35–39.

[59] F.B. Baker, E.K. Storms, C.E. Holly Jr., Enthalpy of formation of zirconium carbide, J. Chem. Eng. Data 14 (1969) 244–246, https://doi.org/10.1021/je60041a034.

[60] A.I. Gusev, A.A. Rempel, A.J. Magerl, Disorder and Order in Strongly Nonstoichiometric Compounds, Springer, 2011.

[61] F. Kazemi, F. Arianpour, H. Rezaie, Kinetic study of carbothermal reduction of zirconia under vacuum condition, J. Therm. Anal. Calorim. 139 (2019) 67–73, https://doi.org/10.1007/s10973-019-08368-5.

[62] L.M. Berger, W. Gruner, E. Langholf, S. Stolle, On the mechanism of carbo-thermal reduction processes of TiO₂ and ZrO₂, Int. J. Refract. Met. Hard Mater. 17 (1999) 235–243, https://doi.org/10.1016/S0263-4368(98)00077-8.

[63] A. Maitre, P. Lefort, Solid state reaction of zirconia with carbon, Solid State Ion. 104 (1997) 109–122, https://doi.org/10.1016/S0167-2738(97)00398-6.

[64] S. Kato, K.I. Ozawa, K. Edamoto, S. Otani, Photoelectron spectroscopy study of the oxidation of ZrC(100), Jpn. J. Appl. Phys. 39 (2000) 5217, https://doi.org/10.1143/JJAP.39.5217.

[65] NIST X-ray Photoelectron Spectroscopy Database, National Institute of Standards and Technology, Gaithersburg MD, 2000, p. 20899. NIST Standard Reference Database Number 20.

[66] I. Bespalov, M. Datler, S. Buhr, W. Drachsel, G. Rupprechter, Y. Suchorski, Initial stages of oxide formation on the Zr surface at low oxygen pressure: an *in situ* fim and XPS study, Ultramiscroscopy 159 (2015) 147–151, https://doi.org/10.1016/j.ultramic.2015.02.016.

[67] G. Greczynski, L. Hultman, Towards reliable X-ray photoelectron spectroscopy: sputter-damage effects in transition metal borides, carbides, nitrides, and oxides, Appl. Surf. Sci. 542 (2021), 148599, https://doi.org/10.1016/j.apsusc.2020.148599.

[68] H. Andren, L. Mattsson, U. Rolander, Atom-probe analysis of zircaloy, J. Phys. 47 (191) (1986) 196, https://doi.org/10.1051/jphyscol:1986228.

[69] H.F. Jackson, W.E. Lee, R. Konigs, R. Stoller, Properties and characteristics of ZrC, in: Comprehensive Nuclear Materials, 1st ed., 2, Elsevier, 2012, pp. 339–372.

[70] Y. Zhang, B. Liu, J. Wang, Self-assembly of carbon vacancies in sub-stoichiometric ZrC₁₋ₓ, Sci. Rep. 5 (2016) 18098, https://doi.org/10.1038/srep18098.

[71] C. Gasparrini, C.J. Richard, D. Horlait, L. Vandeperre, W.E. Lee, Zirconium carbide oxidation: kinetics and oxygen diffusion through the intermediate layer, J. Am. Chem. Soc. 101 (2018) 2638–2652, https://doi.org/10.1111/jace.15479.

[72] R.G.A. Rao, V. Venugopal, Kinetics and mechanism of the oxidation of ZrC, J. Alloy. Compd. 206 (1994) 237–242, https://doi.org/10.1016/0925-8388(94)90042-6.

[73] C. Gasparrini, D. Rana, N. Le Brun, D. Horlait, C.N. Markides, I. Farnan, W.E. Lee, On the stoichiometry of zirconium carbide, Sci. Rep. 10 (2020) 6347, https://doi.org/10.1038/s41598-020-63037-0.

[74] J. Brückner, T. Mäntylä, Reactive magnetron sputtering of zirconium carbide films using Ar-CH₄ gas mixtures, Surf. Coat. Technol. 59 (1993) 166–170, https://doi.org/10.1016/0257-8972(93)90077-2.